Article

Assessment of MODIS, OMI, MISR and CALIOP Aerosol Products for Estimating Surface Visual Range: A Mathematical Model for Hong Kong

Muhammad Imran Shahzad [1,2] , **Janet Elizabeth Nichol [2,*]** , **James R. Campbell [3]** and **Man Sing Wong [2,4]**

[1]   Earth & Atmospheric Remote Sensing Lab (EARL), Department of Meteorology, COMSATS University Islamabad, Park Road, Islamabad 45550, Pakistan; imran.shahzad@comsats.edu.pk
[2]   Department of Land Surveying and Geo-Informatics, The Hong Kong Polytechnic University, Hung Hom, Kowloon, Hong Kong, China; ls.charles@polyu.edu
[3]   Aerosol and Radiation Section, Naval Research Laboratory, Monterey, CA 93943, USA; james.campbell@nrlmry.navy.mil
[4]   Research Institute for Sustainable Urban Development, The Hong Kong Polytechnic University, Hung Hom, Kowloon, Hong Kong, China
*   Correspondence: lsjanet@connect.polyu.hk; Tel.: +44-784-655-6588

check for updates

Abstract: Estimation of atmospheric visibility (VR) using ground and satellite sensors is ineffective under Hong Kong's complex atmosphere and climate. Therefore, the relationship between columnar Aerosol Optical Depth (AOD) from four space-borne sensors (OMI, MODIS, MISR and CALIOP) and B_{ext} from two visibility-recording stations was evaluated, to recommend an effective satellite-based method and spatial resolution, for estimation of VR over Hong Kong. Since most column-integrated aerosol particle extinction occurs within a mixing layer height (MLH) of 1–3 km, column-based AOD from satellites is expected to give a good indication of surface-level conditions, especially when MLH is a known input. The AOD from both MODIS and MISR showed high correlations with B_{ext}; therefore, both were subjected to rigorous statistical analysis along with climatic data to simulate visibility. The best estimate of ground visibility was obtained from MODIS AOD combined with surface-level climatic data, and this explained 84% of the variance in VR, with a low distance error of 0.27 km. Results suggest that the water vapor mixing ratio (Q) alone can explain the combined effect of Atmospheric Pressure (P), Temperature (T) and Relative Humidity (RH) on VR, and that the advection term (VT) alone is sufficient to explain the effects of T, WS and WD on dispersion of aerosols, and hence on VR.

Keywords: visibility; remote sensing; aerosol optical depth; MODIS

1. Introduction

Hong Kong's famed skyline and mountainous horizons are frequently obscured due to poor near-surface visibility, or visual range, which has declined drastically over recent decades. Low visibility is defined specifically as Visual Range (VR) <8 km (Hong Kong Observatory—HKO; [1]). This usually occurs under conditions of high loading of particulate matter (PM), with mean annual aerosol optical depth (AOD) values exceeding 0.60 at 550 nm [2]. Several studies have discussed Hong Kong's limited visibility in the context of local and regional air pollution [3], and whether low visibility is due primarily to transport of regional pollutants under prevailing meteorological conditions [4], local sources [5] or a combination of both [6] is a continuing debate in Hong Kong. Furthermore, there remains uncertainty as to the prevailing optical and physical characteristics of

aerosol experienced under each set of conditions [7,8]. Hong Kong serves as an example of other rapidly urbanizing regions in Asia where industrial and urban development threaten the quality of life, including risks to shipping and air transport due declining visibility. There are many different methods for measuring atmospheric VR, such as transmissometers [9], nephelometers [10], teleradiometers [11], projections based on in situ measurements of aerosol particle mass extinction efficiencies [12] and digital cameras [13]. VR estimates are typically communicated and applied with the presumption of lateral homogeneity relative to the segment of the aerosol layer sampled. However, in reality it is common to find significantly different concentrations of aerosol particle mass in adjoining areas, particularly in urban areas, where lateral covariance will readily perturb in the vicinity of significant source regions [14–16]. Therefore, a method for estimating visibility over a relatively large urban region is necessary to diagnose a regionally representative VR without integrating a singularly focused or in situ result.

Based on advances in satellite-based aerosol remote sensing technologies, many studies have been reported which estimate VR from satellites. Some relevant examples are: (1) the use of satellite-based solar albedo for deriving geometric and optical thickness of fog from the Advanced Very High-Resolution Radiometer (AVHRR) [17]; (2) SOnic Detection And Ranging (SODAR), including a radiative transfer model for calculating the extinction coefficient [18]; (3) the use of luminance and contrast in spatial and frequency domains derived from radiative transfer models from satellite images [19]; (4) atmospheric transmittance derived from satellite AOD measurements [20,21], and (5) the use of statistical regressions with different combinations of band radiances to estimate VR [22]. However, most attempts to derive visibility from satellite data focus only on stratified layers of fog, and all lack rigorous validation, especially for very clear or highly polluted (i.e., high AOD) cases [23–26]. Traditionally, VR values are estimated using Koschmieder's equation (Equation (1); [27]) where, C is the contrast threshold of the human eye (0.02–0.05) based on the health of the eye, and B_{ext} (km^{-1}) is the coefficient of extinction for light coming from the object to the eye.

$$VR = \frac{\ln C}{B_{ext}} \tag{1}$$

Most previous studies have either used columnar AOD (Equation (2); [12]) or PM proxies (Equation (3); [23,28]) for estimating B_{ext}.

$$AOD = \int_0^z B_{ext}\ (RH(z))\ dz \tag{2}$$

$$AOD = \left[\int_0^z \frac{B_{ext}\ (RH(z))}{B_{ext}\ (RH(z_0))}\ dz \right] \frac{3}{4}\ PM(z_0)\ \frac{f(RH(z_0))}{\rho}\ \frac{Q_{dry}}{r_{eff}} \tag{3}$$

Here, $RH(z_0)$ and $RH(z)$ are the relative humidity at and above surface height, Q_{dry} is the extinction efficiency under dry conditions, r_{eff} is the effective radius and ρ is the aerosol mass density [28]. It is important to note that the AOD-PM relationship (Equation (3)) involves many complicated factors, whereas a relatively simple AOD-VR relationship can be derived by comparing Equations (1) and (2) (Equation (4)), where Z is the scaling height based on the shape of aerosol extinction profile.

$$AOD = \frac{\ln c}{VR}\ Z \tag{4}$$

Due to the robustness of satellite-derived AOD algorithms, AOD has been used in environmental monitoring for the retrieval of ground level fine particulates (PM2.5), although the relationship between AOD and PM2.5 is often complex [29]. However, estimating VR from satellite-based aerosol observations is potentially simpler than PM2.5 due to the simplicity of the AOD-VR relationship (Equation (4)) [23,28]. Despite this, more investigation is needed to parameterize the relationship

between AOD and VR effectively for an atmospherically complex region such as Hong Kong. Uncertainties may arise in the AOD-VR relationship due to cloud contamination, inappropriate selection of the aerosol model in a complex region, and heterogeneous surface reflectance [30,31]. In addition, the column-integrated values of AOD may not adequately represent the near surface aerosols responsible for visibility reduction [32]. Therefore, although the AOD_VR relationship is simple, the retrieval of AOD to represent VR at a certain level is more complex, and requires additional parameters. For these reasons, the above-mentioned studies have shown large bias on very clear or highly polluted days. Therefore, currently there is no method for bridging the data gaps in Hong Kong and globally, which are due to the coarse deployment of ground instruments [19,23].

Therefore, to investigate the potential for using satellite AOD products to estimate VR, we evaluate AOD products from different sensors for those AOD pixels corresponding with VR monitoring stations in and around Hong Kong. The objectives of this study then, are to: (1) evaluate the potential of space-borne optical sensors for remote sensing of VR at surface level; (2) identify the most suitable spatial resolution for monitoring VR; (3) identify the climatic parameters required for estimating VR from satellites by examining the relationship between surface-level VR, columnar AOD and climatic data. The ultimate objective is to provide a numerical model, based on real-time AOD values and corresponding climate data, for providing more accessible and routine visibility information to defense and civil authorities.

2. Study Area, Materials and Methods

2.1. Study Area

Hong Kong occupies a land area of 1100 km^2, of which only approximately 30% is urban. It is in a sub-tropical region, surrounded by the South China Sea to the east, south and west, and bordering Shenzhen, China to the north (Figure 1). The local VR is, perhaps surprisingly, highest during the hot humid summer, with southerly winds from the South China Sea, and lowest in the winter and spring, with dry northerly winds from continental China [33]. These winds in the winter dry season negatively affect the VR in Hong Kong due to massive urban and industrial development in the adjacent Chinese mainland, accompanied by growth in polluting factory outputs, construction site and power plant operations, all of which increase the aerosol particle loading.
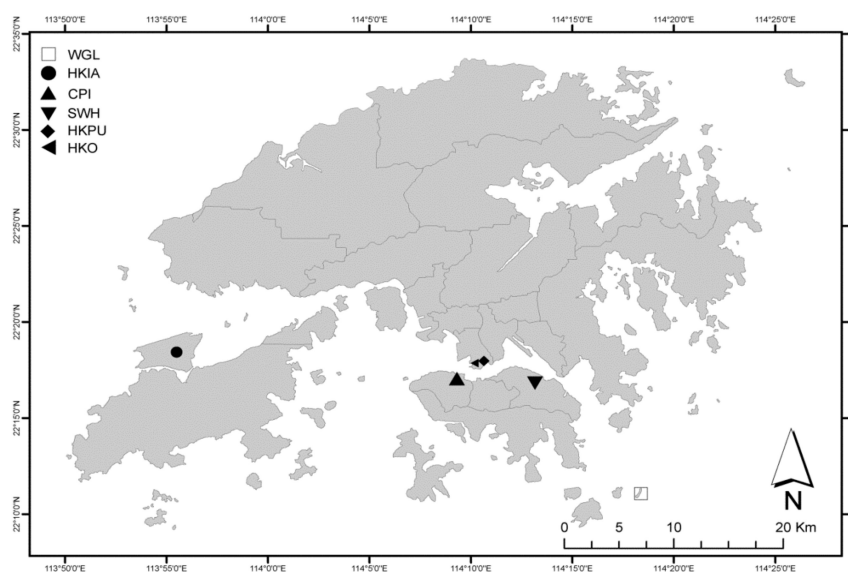

Figure 1. Study area and locations of the visibility monitoring stations.

2.2. Materials

2.2.1. Satellite-Based Aerosol Observations

We consider Level 2 satellite *AOD* products from four sensors (Table 1), namely: (1) the Collection 5 AOD data from of NASA's MODerate Resolution Imaging Spectroradiometer (MODIS) aerosol products (MOD04 and MYD04) at 550 nm with 10 km^2 resolution, between 2000 and 2009 [34]; (2) the Multi-angle Imaging SpectroRadiometer (MISR) AOD products at 558 nm with 17.6 km^2 resolution between 2005 and 2009 [35]; (3) the OMAERO aerosol product at 483 nm with 27.8 km^2 resolution derived from the Ozone Monitoring Instrument (OMI) from 2004 to 2009 [36]; and (4) the Cloud-Aerosol LiDAR with Orthogonal Polarization (CALIOP) 5 km AOD L2-APro product at 532 nm from 2006 to 2009 [37]. We did not use vertical profile data from CALIOP, to remain consistent in our approach for comparing different aerosol products, because other AOD products do not have vertical profiles. These AOD products in the green or near-green regions of the visible spectrum are compared with hourly observer estimates of VR from the two ground stations, the Hong Kong Observatory (HKO) and the Hong Kong International Airport (HKIA), as described in next sections.

Table 1. Spatial and temporal resolution of satellite AOD products used in the study.

Source	Spatial Resolution	Wavelength (nm)	Temporal Resolution
MODIS	10 km	550	Daily
MISR	17.6 km	558	7–9 days
CALIOP	5 km	532	16 Day
OMAERO	27.8 km	342	Daily

The use of satellite-based AOD products for global air quality monitoring is now well established. Accordingly, studies have reported errors for AOD products for MODIS ($\pm 0.05 \pm 20\%$ * AOD [30]), OMI (20%; [38]), MISR (20%; [39]), and CALIOP ($\pm 0.05 \pm 40\%$ * AOD [37,40]). Localized uncertainties, particularly surrounding a humid coastal city such as Hong Kong, are exacerbated by heterogeneous surface reflectance, mixed aerosol optical characteristics, and strong shallow water and ocean color gradients [29,41]. Hong Kong frequently experiences several aerosol types within any given sampling location, as reported by many studies [29,41,42]. Therefore, the South China Sea region, including Hong Kong, is recognized as an area where relatively large derived-AOD errors occur [30]. Therefore, this study proposes a numerical model to resolve the effect of these inherent errors in estimation of VR using climatic data in addition to operational AOD products.

2.2.2. Visual Range and Climate Data

In addition to AOD, we consider multiple thermodynamic and physical parameters measured at the surface for a better understanding of the AOD-VR relationship, since meteorological conditions affect particle mass concentrations, and thus the optical and physical properties of pollutants that influence VR [43]. Certain meteorological conditions depending on prevailing temperature (T), pressure (P), relative humidity (RH), wind speed (WS) and direction (WD) can bring in and/or sweep out aerosols in a region. On the other hand, optical and chemical properties of the aerosols can also be drastically altered in a stagnant atmosphere. Therefore, we used T, P, RH, WS and WD, vector components of wind towards East (U) and North (V), Mixed-Layer Height (MLH), water vapor mixing ratio (Q), and temporal changes in T and P (ΔT and ΔP). The available datasets were collected by HKO from 2005 to 2008.

RH affects particle size distribution through deliquescence, which is seen most significantly in smaller, fine-mode particles (<1 μm). This effect further influences scattering cross-sections inherent to a given aerosol particle layer [44]. Preliminary analysis for this study (not shown here) indicated that correlation between AOD and VR decreases with an increase in RH until RH = 90%, because the given fine-mode particles grow enough to scatter or absorb more light under increasing

RH. This finding is consistent with other studies [45]. Therefore, data corresponding to RH greater than 90%, and particularly those associated with measurable rainfall, were excluded from the analysis.

It is well known that seasonal variation in air quality near Hong Kong is due to corresponding regional shifts in cyclonic and anticyclonic synoptic circulation, alternately advecting fresh and polluted air to the region, respectively [46,47]. To quantify the effect of wind, Wu et al. [48] used 'wind flux' derived from MLH, and the vector U and V wind components measured by a wind profiler. This enabled them to study the combined effect of MLH and WS at different heights to better understand the vertical dispersion of aerosol particles nearby. We adopt a similar analysis here.

Relatively high surface temperatures correlate with processes that induce aerosol particle dispersion, primarily through thermal turbulence and convection, thus increasing VR [33,43]. Change in temperature, wind speed and direction result in atmospheric instability and play an important role in dispersion or advection of aerosols at regional level. Therefore, advection terms, UT and VT (products of T with U and V), temporal change terms, ΔT and ΔP, along with Q, which itself is a function of P, T and RH, can also be reasonable indicators for convection, expansion of the MLH and thus dispersion of aerosol particles relative to the surface. Therefore, UT, VT, ΔT, ΔP and Q become primary parameters for characterizing conditions responsible for VR at any given site and time, locally.

The MLH serves as a scaling height, since most column-integrated aerosol scattering occurs within an MLH of 1 to 3 km, regionally [49]. MLH in Hong Kong is estimated twice daily (0800 HKT and 2000 HKT) by radiosonde at King's Park ($22°18'43''$, $114°10'22''$; 65 m above mean sea level—MSL). Since there is a two to three-hour difference in the time of sounding and the daylight satellite overpass (1030 local time), during which MLH can change significantly, MLH data from radiosonde are not included in this study. Instead, MLH data corresponding to the satellite pass time are estimated from NCEP FNL Operational Model Global Tropospheric Analyses datasets, which we consider accurate to within 500 m, and thus reasonable for our purpose.

Surface VR is measured operationally at six locations in Hong Kong, by qualified weather observers, as well as by forward-scattering radiometers and transmissometers (Figure 1; Table 1). Although these monitoring sites have contributed to some characterization of regional VR, they are still considered insufficient for depicting VR conditions over all of Hong Kong. VR observations conducted by trained observers from HKO and HKIA are used here to evaluate the AOD-VR relationship for each sensor and later to validate the proposed numerical model.

2.3. Methods

This study is conducted in two parts after converting VR values from HKO and HKIA to B_{ext} using Equation (1). Firstly, the simple AOD-B_{ext} relationship is analysed to evaluate the potential of satellite-based estimates of VR, and to identify the most appropriate satellite-estimated AOD product currently available for estimating VR. The relationship is analyzed in terms of correlation coefficient (R), root mean square error (RMSE) and mean absolute deviation (MAD). Secondly, numerical models based on the combination of meteorological data and satellite-based AOD are tested to simulate VR.

2.3.1. Evaluation of Satellite Sensors

The OMI, MODIS, MISR, and CALIOP AOD products are compared with B_{ext} observations at HKO and HKIA within a period of ± 30 min of the overpass time [50]. The VR can vary significantly over time and space. For example, at any given time, VR may be greater or smaller than the standard spatial resolution of an AOD product. Such variation can affect the underlying relationship of VR with the AOD product at any given spatial resolution. Therefore, the AOD from each sensor is extracted at HKO using kernels (K) of 1-by-1, 3-by-3, 5-by-5 pixels, and so on, until the kernel size is greater than or equal to 50-by-50 km^2. A maximum kernel size of 50-by-50 km^2 is used, since surface observations throughout the study period indicate that VR in Hong Kong does not exceed 50 km. In addition, a kernel window greater than 50-by-50 km^2 would be unable to decouple the AOD extracted at the HKO and HKIA ground visibility measurement sites, since the two stations are approximately 35 km

apart. The variable kernel size helps to select an optimal spatial window for a given satellite AOD product, and to understand its relationship with surface-level VR.

2.3.2. Estimating Surface Visibility

After selecting the operational satellite AOD products exhibiting the best overall representation of B_{ext}, these are then tested for simulating VR using numerical modeling. The selected AOD products are correlated with corresponding climate data for 2005 to 2008 within a period of ± 30 min of any given overpass time. Data for 2005 to 2007 are used to build an empirical model for simulating VR or B_{ext} using the satellite-based AOD product, and data for 2008 are then used to evaluate the result. Evaluation of the model is done for both HKO and HKIA locations. Several transformations are applied to VR and B_{ext}, as well as the independent variables (AOD, T, P, RH, ΔT, ΔP, U, V, Q, MLH, WS, VT, UT and WD) to acquire normal distributions before statistically evaluating the overall result. These transformations also attempt to contain non-linearity among parameters, where applicable. These transformations include square root (sqrt), natural logarithm (ln), square (sqr) and inverse (inv) transformations. This results in ten dependent and fifty-five independent variables, where a variable with the lowest Anderson-Darling statistics (AD value) will show normal distribution [51]. The independent and dependent variables with the highest significant correlation coefficients (*p*-value < 0.1) and the lowest AD values are grouped together as potential candidates for multiple linear regression, because correlation alone cannot completely imply a cause-and-effect relationship. The variable with the minimum AD value is included in the regression, because its distribution would be more normal than others. The condition of *p*-value less than 0.1 is imposed to select enough independent variables to be analyzed with regression modeling.

Each group of variables is subjected to multiple linear regression, and their *p*-value, T statistic, F statistic, variance inflation factor (VIF), coefficient of determination (R^2) and error in prediction (PRESS) are analyzed. Independent variables with significantly larger *p*-values and VIFs, as well as variables with smaller T and F statistics, are omitted one by one, and regression is repeated until all variables correspond to *p*-value < 0.001. The basic assumptions of regression (variance of the error population should be constant, and residuals are independent and normally distributed) are validated by analyzing the standard residual plot and Durbin-Watson statistics (DWS), where the residual should be randomly distributed without any pattern in their spread, and DWS should be near 2.0 [52].

Each statistical set satisfying the above criteria is further subjected to 'stepwise' [53] and 'best subset' regression [54]. Stepwise regression adopts a single path through the independent variables, whereas best subset regression explores all pathways to select the best combination of independent variables. Therefore, a regression model with '*n*' variables developed, using the 'best subset' approach, is expected to perform better than one with the same number of variables developed using a stepwise approach. As a result, the set of variables selected using stepwise regression is also analyzed with 'best subset' regression. A model is selected for application if the *Cp*-value is approximately equal to the number of independent variables in it (Equation (5); [55]).

$$Cp = \frac{SSE}{MSE} - N + 2n \tag{5}$$

where *SSE* is the sum of square errors of the model with '*n*' parameters, including independent variables and intercept; *MSE* is the mean square error of the model recommended by stepwise regression; and *N* is the number of samples. The selected model is then tested using the validation data from the year 2008.

3. Results

3.1. AOD-B_{ext} Relationship

For kernel sizes of both 1-by-1 and 3-by-3 pixels, as well as at both VR stations, correlations between OMI AOD and B_{ext} are lower than for other sensors, with R = 0.30 and 0.24 at HKIA (Figure 2)

and R = 0.42 and 0.39 at HKO (Figure 3), respectively. These relatively low correlations may be due to the frequent overestimation of OMI AOD due to sub-pixel cirrus cloud contamination at the low (28 km) OMI resolution [56], as reported by [28,43]. That is, the OMI pixel size of 27.8 km^2 can easily be mixed with thin-cloud cover, particularly in the vicinity the South China Sea region, where cirrus cloud frequencies are relatively high [57], and thus an underestimate of single scattering albedo occurs [58]. Additionally, the OMI AOD is reported at 483 nm, which is expected to experience more extinction than the human observation. This may also be the cause of high bias for OMI extinction.
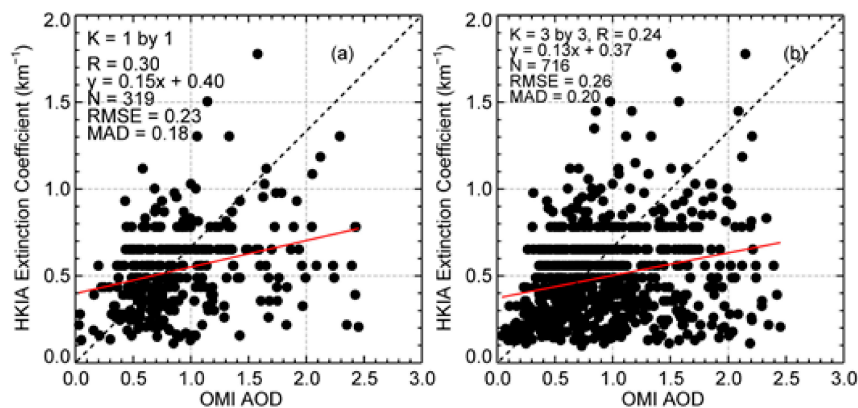

Figure 2. Correlation of B$_{ext}$ at HKIA with OMI AOD (27.8 km product at 483 nm) for kernel window of (**a**) 1 by 1 and (**b**) 3 by 3. Dashed line represents a 1:1 line, whereas solid line is the resultant regression line.
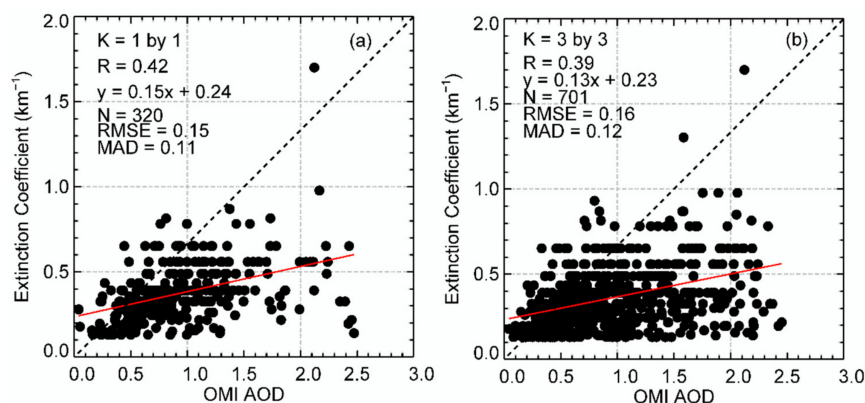

Figure 3. Like Figure 2, but at HKO.

Low correlations are also observed between CALIOP AOD and B$_{ext}$ at both HKO (R = 0.47 and 0.17 for kernel windows of 9-by-9 and 11-by-11 pixels respectively; Figure 4a–c) and HKIA (R = 0.32, 0.39, 0.25, 0.30, 0.24 and 0.12 for kernel windows of 1-by-1 to 11-by-11 pixels, respectively; Figure 5a–f). It is important to note that all correlations are reported after excluding the potential outliers due to high AOD, which are highlighted in each figure as red asterisks. Furthermore, these outliers likely reflect unscreened artifacts and mixed pixels. Therefore, they can be treated as erroneous readings. These readings are not, however, excluded in designing the model for estimating visibility in the later part of the methodology. Low correlations from CALIOP may be due to its limitations in collecting data from near ground level during the day because of a lower signal-to-noise ratio in the presence of high solar background [59]. To overcome this problem, the CALIOP team uses a nighttime calibration constant to derive the daytime profiles. Even with this amendment, CALIOP is reported to underestimate AOD by a factor of two compared with AOD from a ground-based AERONET sunphotometer [60].
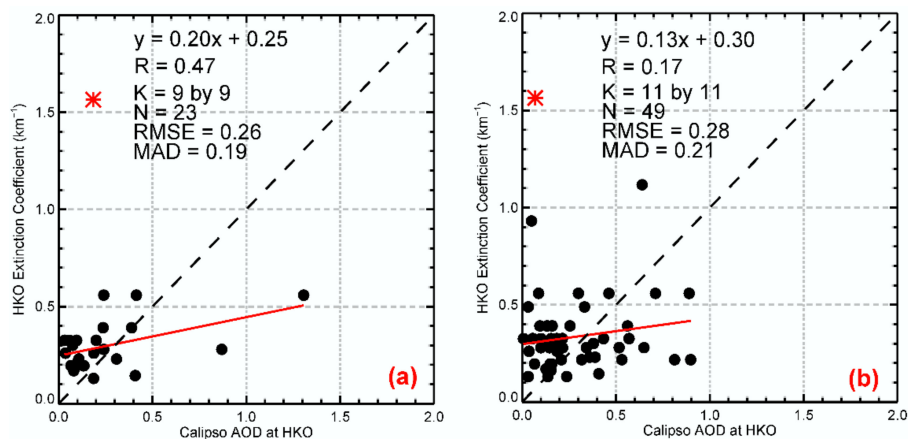
Figure 4. Correlation of Extinction Coefficient at HKO with CALIOP AOD (5 km product at 532 nm) for kernel windows of (**a**) 9 by 9 and (**b**) 11 by 11. There is no valid AOD retrieval for kernel windows of 1 by 1 to 7 by 7. *—potential outlier in the data. Lines as described in Figure 2.
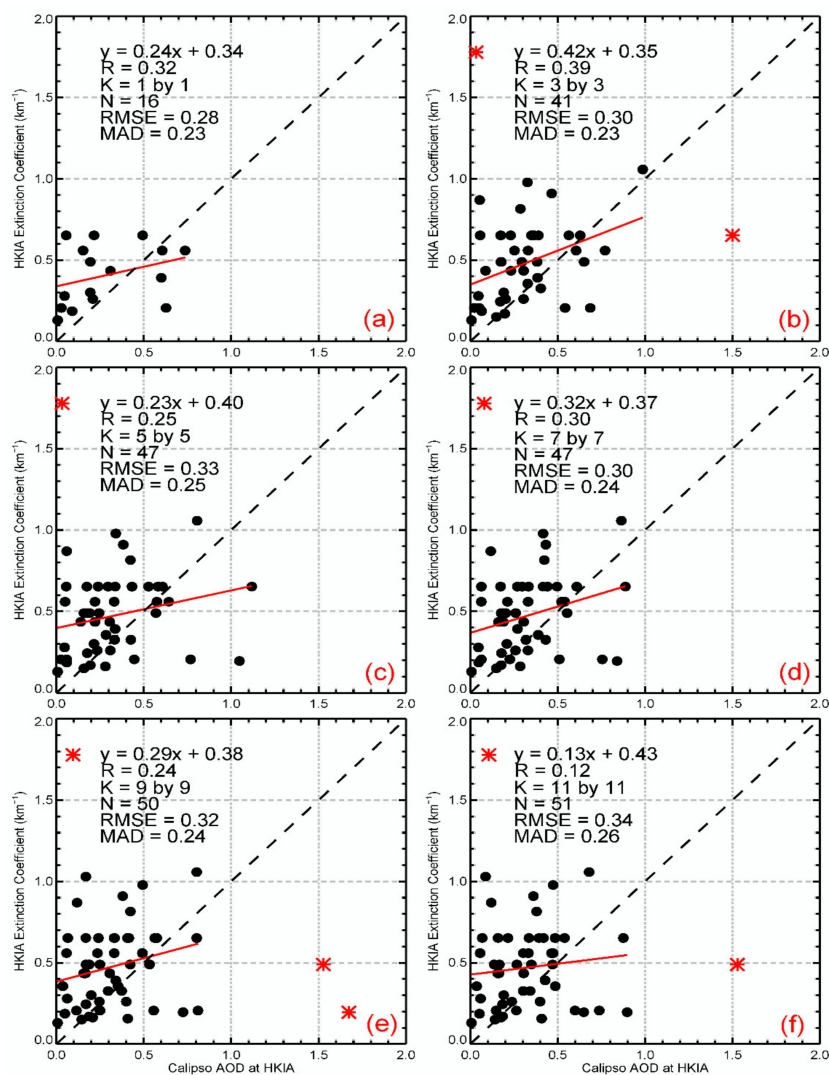

Figure 5. Like Figure 4, but at HKIA for kernel windows of (**a**) 1 by 1 (**b**) 3 by 3 (**c**) 5 by 5 (**d**) 7 by 7 (**e**) 9 by 9 and (**f**) 11 by 11.

For MISR, the correlation between AOD and B_{ext} for kernel windows of 1-by-1 and 3-by-3 pixels, respectively, are 0.60 and 0.51 at HKIA (Figure 6a,b), and 0.26 and 0.63 at HKO (Figure 7a,b). The better results for the urban HKO site, with higher correlation, lower MADs and RMSEs, than for the coastal HKIA site agree with the findings reported by Liu et al. [61] and Jiang et al. [62] in China. The MISR AOD exhibits higher correlation with B_{ext} than OMI and CALIOP, which may be because the MISR AOD retrieval algorithm incorporates a large number of aerosol models, with mixtures from different aerosol parameters including shape, size and mass [63], thus the AOD product is more robust.
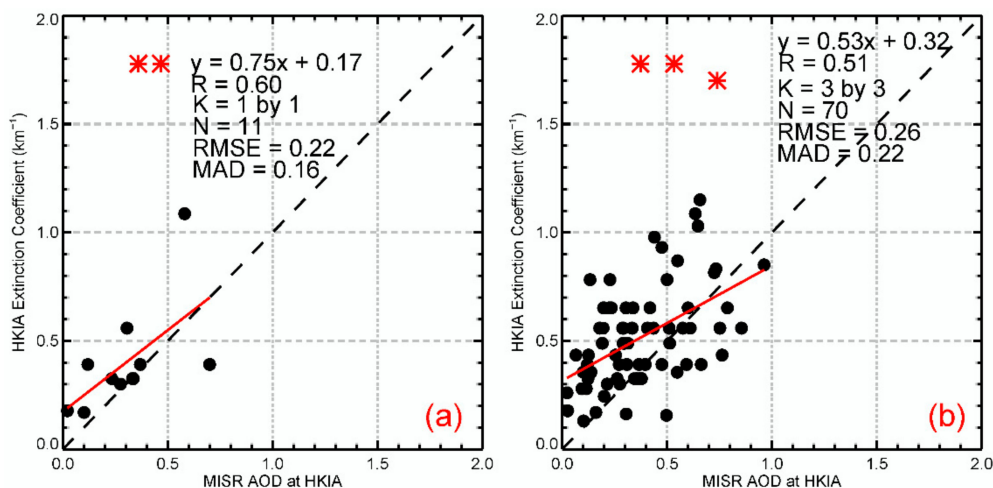

Figure 6. Correlation of Extinction Coefficient at HKIA with MISR AOD (17 km product at 558 nm) for kernel windows of (**a**) 1 by 1 and (**b**) 3 by 3. *—potential outlier in the data. Lines as described in Figure 2.
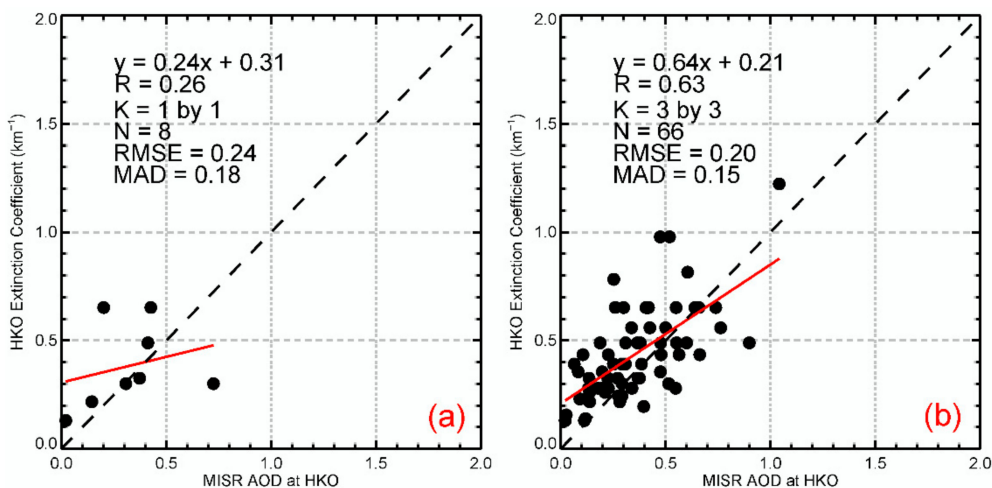

Figure 7. Like Figure 6, but at HKO, (**a**) 1 by 1 and (**b**) 3 by 3.

Like MISR, the MODIS AOD performs better at the urban HKO site than at the coastal HKIA (Figure 8). The correlations between MODIS AOD and B_{ext} at HKO are 0.38, 0.51 and 0.53 for kernel windows (K) of 1-by-1, 3-by-3 and 5-by-5, respectively (Figure 8d–f), compared with 0.11, 0.35 and 0.26 (Figure 8a–c) at HKIA.
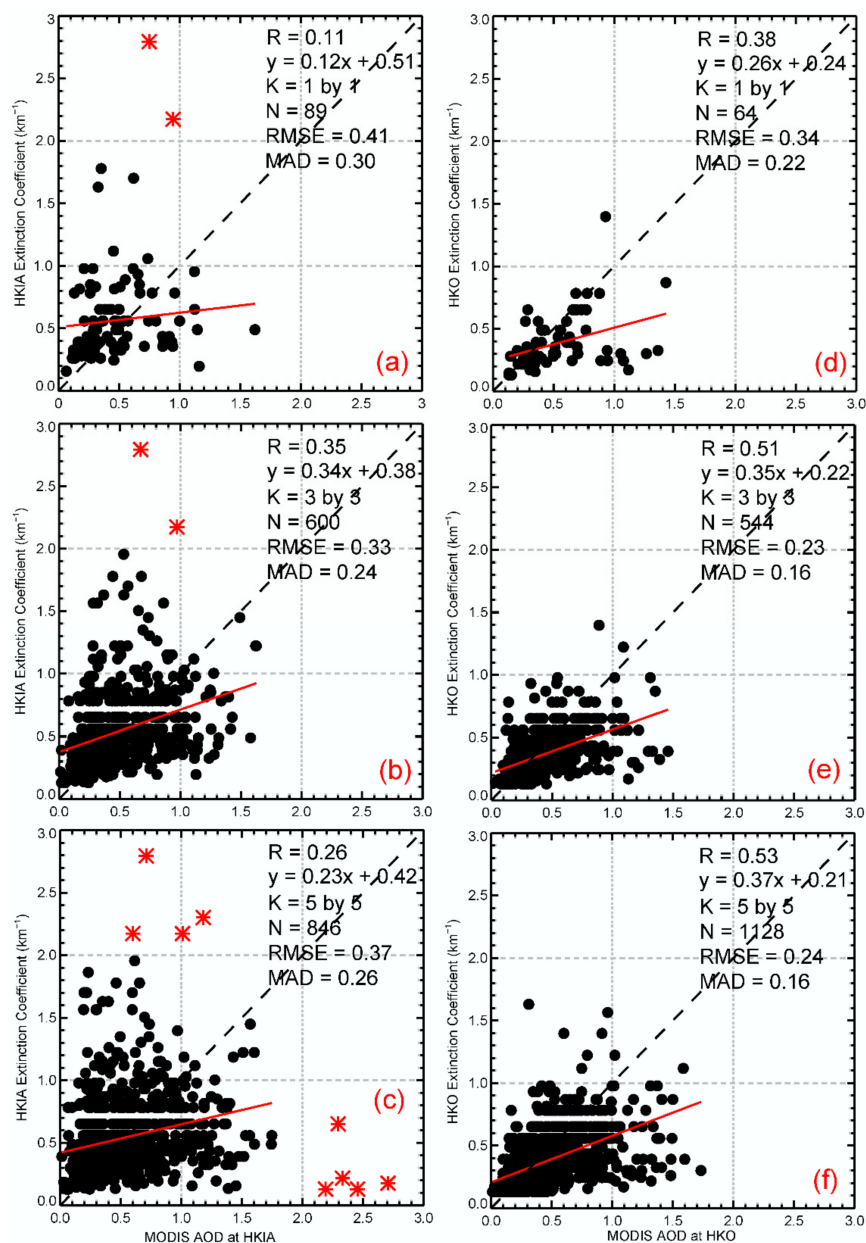
Figure 8. Correlation of Extinction Coefficient with MODIS AOD (10 km product at 550 nm) for HKIA (**a**–**c**) and HKO (**d**–**f**) for kernel windows of 1 by 1 (top row), 3 by 3 (middle row) and 5 by 5 (bottom row). *—potential outlier in the data. Lines as described in Figure 2.

3.2. Summary of Sensor Performance

Great differences are observed in the R, RMSE and MAD between coastal (HKIA) and urban (HKO) areas (Figure 9). Figure 9 compares the R, RMSE and MAD at HKIA and HKO for increasing spatial resolution in the four sensors. The highest correlation at HKIA is for MISR AOD for kernel window of 1-by-1 (R = 0.60), followed by MISR AOD for kernel windows of 3-by-3 (R = 0.51) and CALIOP for kernel window of 3-by-3 (R = 0.39) (Figure 9 top). However, the highest correlation at HKO is for MISR AOD for kernel window of 3-by-3 (R = 0.63), followed by MODIS AOD with kernel windows of 5-by-5 (R = 0.53) and 3-by-3 (R = 0.51), respectively (Figure 9 top).
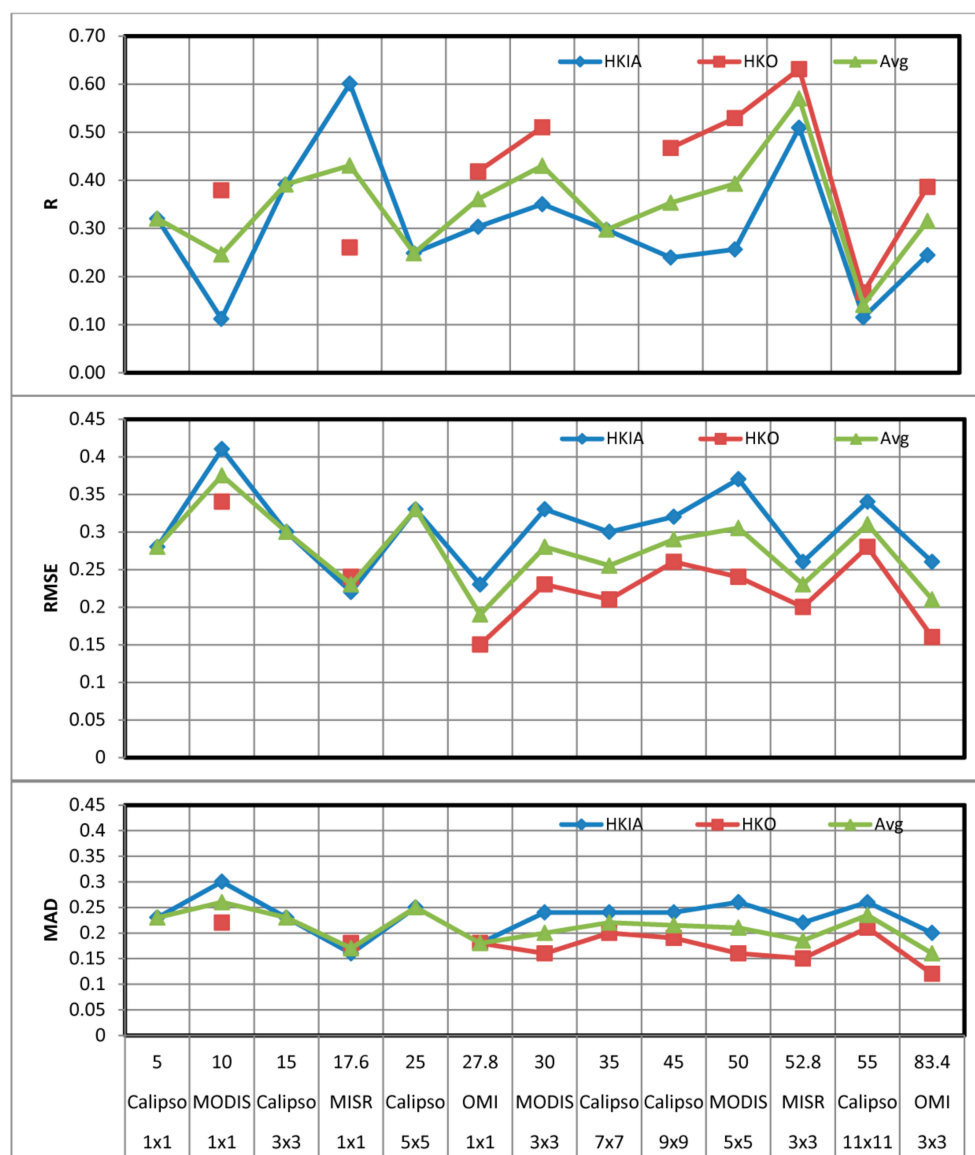
Figure 9. Variations in R (**top**), RMSE (**middle**) and MAD (**bottom**) at different spatial resolutions of MISR, MODIS, OMI and CALIOP for HKIA, HKO, and their Average. Spatial resolution (km), names of sensors and sizes of kernel window are labelled in the first, second and third *x*-axis, respectively. The scales of R, RMSE and MAD are on the y-axis. Negative correlation values for CALIOP AOD are not shown.

Hence, the MISR AOD exhibits the highest correlation with surface level extinction coefficient, followed by MODIS. MISR also has a lower RMSE and MAD at both HKO and HKIA than other sensors. Although the correlation, RMSE and MAD at both HKO and HKIA for MISR are slightly higher than for MODIS, the high temporal resolution of MODIS (daily, compared with 7–9 days) along with its comparable RMSE and MAD to MISR, makes it a more practical sensor for operational estimation of surface visibility in Hong Kong. Indeed, only 70 measurements for MISR AOD were available over the whole study period, and this would not be adequate for operational visibility monitoring, which is one of the main objectives of this study. Therefore, further analyses used MODIS AOD products for kernel windows of 5-by-5.

3.3. Estimation of Surface Visibility

MODIS AOD data for a kernel window of 5-by-5 and B_{ext} at HKO are segregated into training (years 2002 to 2006 and 2008) and validation sets (years 2007 and 2009) to estimate and validate the retrieved MODIS B_{ext}. Like Figure 8, the training data set also showed significant correlation between MODIS AOD and B_{ext} at HKO (Equation (6); Figure 10a), as

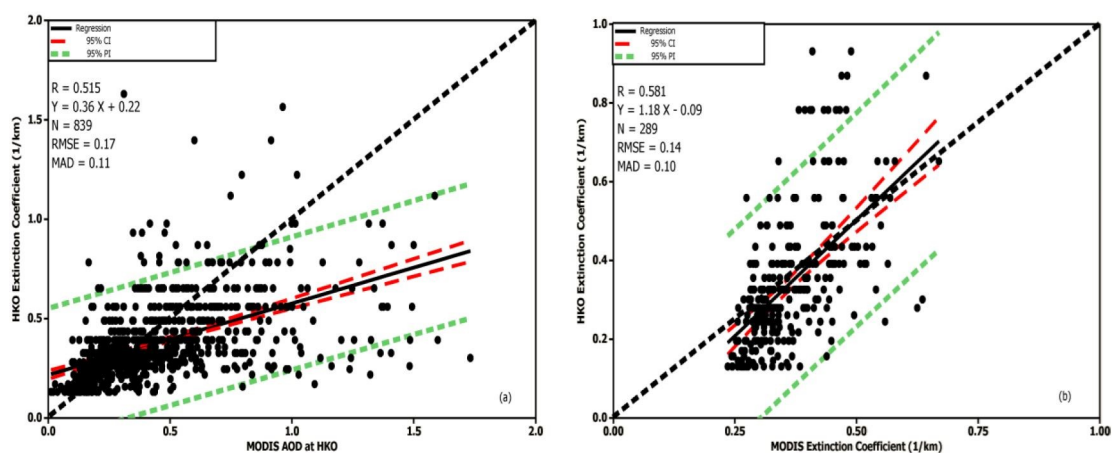$$B_{ext} = 0.36 \text{ (MODIS AOD)} + 0.22 \tag{6}$$

Figure 10. Correlation of Extinction Coefficient with MODIS AOD (10 km product at 550 nm) using Model-1 for HKO: (**a**) linear regression of training data for the years 2002 to 2006 and 2008; (**b**) estimated MODIS extinction coefficient using MODIS AOD from years 2007 and 2009. Black dashed line represents a 1:1 line, whereas black solid line is the resultant regression line.

Consequently, Equation (6) is designated as Model-1 (M1) and tested against the validation data set (Figure 10b). Most of the validation data points fell outside the 95% confidence interval, indicating a weak estimation power for M1. Therefore, it was hypothesized that the estimation of B_{ext} might improve further by adding climatic data in a multiple linear regression model.

3.4. Time Series Analysis

For ease of analysis, the values of the climatic variables P, T, VT, Q, RH and AOD were smoothed and standardized to between -1 and $+1$ (Figure 11). The relationships between P, T, RH, VT, AOD and Q can explain the variations in visibility in terms of subsidence and uplift of the aerosols. The relationship is shown to be seasonal, with highest visibility in summer and lowest in winter. Overall, VR increases with decreasing P, RH and AOD. This is because low pressure generally makes the atmosphere unstable, generating convective winds, which may shorten the aerosol residence time whereas low RH decreases the aerosol's scattering efficiencies by inhibiting the increase in aerosol size.

Also, VR further increases with increasing T, VT and Q, as low temperatures indicate the prevalence of the winter continental northeast monsoon, bringing regional anthropogenic aerosols to Hong Kong and reducing the VR. In contrast, high temperatures are associated with summer and early autumn, bringing clean and fresh maritime winds from the southwest [33]. It is also noted that the hours with reduced visibility in winter and summer are associated with "$-$VT" and "+VT". Indeed, a total 78% of the hours of reduced visibility during the study period are associated with "$-$VT" due to advection of aerosols from the north and northeast. Hence, VT can explain the effect of WS, WD and T.
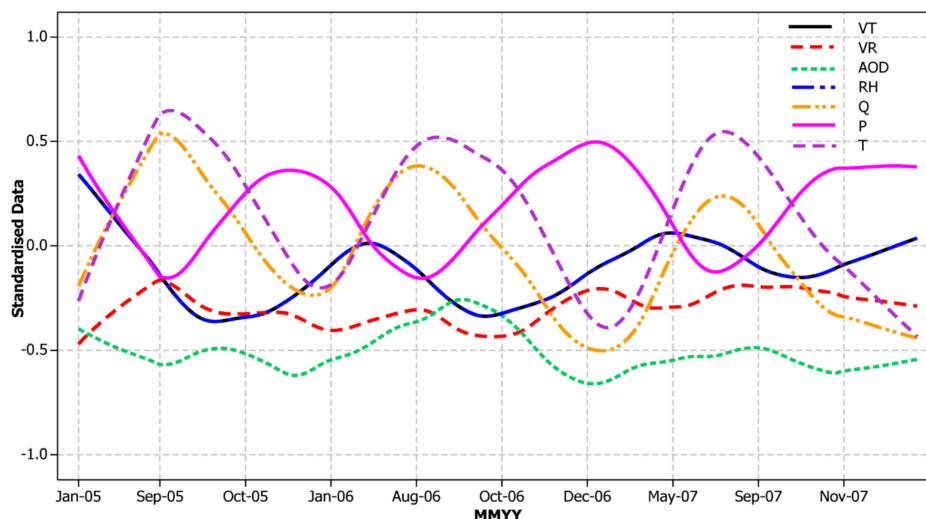
Figure 11. Line plot of smoothed and standardized VR, AOD, RH, VT, Q, P and T, where VT and RH are overlapping throughout the study period. NB. The *x*-axis shows only dates with available time-matched data, and thus is nonlinear.

Furthermore, it is also evident that VR increases with increasing Q. A high value of Q indicates an unstable atmosphere, increasing the vertical and horizontal aerosol dispersion. Usually a high value of Q suggests warmer weather conditions. Low values of Q are commonly associated with the cold season and/or cold air masses that lower the MLH, bringing aerosols into the lower atmosphere. This increases the air density and decreases the VR. Hence, Q helps to explain the combined effect of T, P and RH on VR.

3.5. Parameterization of the AOD-VR Relationship

Correlation analysis is used to explore the relationship between B_{ext}, VR and the climate parameters described above. The correlation matrix for ten dependent and fifty-five independent variables from the training data set (as discussed in methodology) is analyzed to select potential parameters for constructing a regression model using climatic data and MODIS AOD at HKO. Part of the correlation matrix containing potential parameters, is shown in Table 2 and the respective *p*-values are italicized in the line following each variable.

Some of the transformations were able to improve the correlations. For example, the correlation between B_{ext} and AOD improved from 0.78 to 0.79 when B_{ext} and AOD were transformed into $\ln(B_{ext})$ and $\ln(AOD)$. Similarly, correlation between VR and AOD improved from -0.74 to -0.80 when VR and AOD were transformed into $(VR)^{1/2}$ and $\ln(AOD)$. This is because Visibility and AOD are non-linearly inversely proportional, and the transform converts the non-linearity effect to linearity. A few parameters, such as MLH, did not show significant correlation with visibility. This may be because the atmosphere of Hong Kong is not clean above the MLH, due to mountain lofting of local pollution and the huge amount of vertical lofting from shipping emissions in both Hong Kong and Shenzhen [47]. The parameters with the highest correlation and lowest *p*-value from each column were selected for constructing a multiple linear regression model, followed by stepwise and best subset regression models as described in the methodology. Because the regression models denoted with bold variables in Table 2 performed far better than the rest, only those models are discussed hereafter.

As a first attempt, all the selected variables (bold variables in Table 2) were subjected to regression analysis to propose an optimal model (Full model). The Full model gave a poor fit, where some of the independent variables with significant correlation (Table 2) turned out to be insignificant (Table 3), since the *p* values for UT, VT, U, V, $(T)^2$ and $(P)^2$ were not significant at 0.01, with the largest Variance Inflation factor (VIF) of 68.52 being for T^2. It is to be noted that a VIF close to zero shows no, or

minimum, co-linearity among the regression variables. Hence, a regression variable, $(T)^2$, was dropped from the model and the regression was repeated for the remaining variables. The new model was designated as Model A. This time $(P)^2$ was omitted due to the reasons explained earlier, and the process was repeated until a significant Model E was achieved. The regression statistics of each model are shown in Table 3.

Table 2. Correlation matrix for independent and dependent variables.

	VR	$(VR)^{-1}$	$(VR)^2$	$(VR)^{1/2}$	$ln(VR)$	B_{ext}	$ln(B_{ext})$	$(B_{ext})^{1/2}$	$(B_{ext})^{-1}$	$(B_{ext})^2$
AOD	−0.74	0.78	−0.66	−0.76	−0.78	0.78	0.78	0.78	−0.74	0.74
	0.00	*0.00*	*0.00*	*0.00*	*0.00*	*0.00*	*0.00*	*0.00*	*0.00*	*0.00*
T	0.12	−0.08	0.13	0.11	0.10	−0.08	−0.10	−0.09	0.12	−0.07
	0.09	*0.23*	*0.06*	*0.12*	*0.15*	*0.23*	*0.15*	*0.19*	*0.09*	*0.31*
P	−0.11	0.05	−0.13	−0.09	−0.08	0.05	0.08	0.07	−0.11	0.03
	0.13	*0.46*	*0.07*	*0.18*	*0.26*	*0.46*	*0.26*	*0.35*	*0.13*	*0.66*
RH	−0.08	0.16	−0.04	−0.10	−0.13	0.16	0.13	0.15	−0.08	0.19
	0.25	*0.02*	*0.57*	*0.14*	*0.07*	*0.02*	*0.07*	*0.04*	*0.25*	*0.01*
MLH	0.01	−0.07	−0.02	0.03	0.04	−0.07	−0.04	−0.05	0.01	−0.08
	0.88	*0.35*	*0.81*	*0.72*	*0.57*	*0.35*	*0.57*	*0.44*	*0.88*	*0.26*
UT	−0.15	0.18	−0.13	**−0.16**	−0.17	0.18	0.17	0.18	−0.15	0.18
	0.03	*0.01*	*0.06*	***0.02***	*0.01*	*0.01*	*0.02*	*0.01*	*0.03*	*0.01*
VT	0.21	−0.18	0.21	**0.21**	0.20	−0.18	−0.20	−0.19	0.22	−0.14
	0.00	*0.01*	*0.00*	***0.00***	*0.00*	*0.01*	*0.00*	*0.01*	*0.00*	*0.04*
Q	0.11	−0.02	0.15	0.09	0.07	−0.03	−0.07	−0.05	0.11	0.01
	0.11	*0.73*	*0.03*	*0.20*	*0.33*	*0.73*	*0.33*	*0.52*	*0.11*	*0.91*
U	−0.17	0.20	−0.14	**−0.18**	−0.19	0.20	0.19	0.19	−0.17	0.20
	0.02	*0.00*	*0.05*	***0.01***	*0.01*	*0.00*	*0.01*	*0.01*	*0.02*	*0.00*
V	0.18	−0.15	0.18	**0.18**	0.17	−0.15	−0.17	−0.16	0.18	−0.13
	0.01	*0.03*	*0.01*	***0.01***	*0.01*	*0.03*	*0.01*	*0.02*	*0.01*	*0.07*
WD	0.02	0.03	0.05	0.01	0.00	0.03	0.00	0.02	0.02	0.05
	0.73	*0.66*	*0.49*	*0.88*	*0.96*	*0.66*	*0.96*	*0.80*	*0.73*	*0.44*
WS	0.00	−0.06	−0.01	0.02	0.03	−0.06	−0.03	−0.05	0.00	−0.10
	0.95	*0.36*	*0.87*	*0.82*	*0.67*	*0.36*	*0.67*	*0.51*	*0.96*	*0.15*
ln(AOD)	−0.79	0.74	−0.76	**−0.80**	−0.79	0.74	0.79	0.77	−0.79	0.67
	0.00	*0.00*	*0.00*	***0.00***	*0.00*	*0.00*	*0.00*	*0.00*	*0.00*	*0.00*
ln(RH)	−0.09	0.16	−0.05	**−0.11**	−0.13	0.16	0.13	0.15	−0.09	0.19
	0.21	*0.02*	*0.50*	***0.12***	*0.06*	*0.02*	*0.06*	*0.03*	*0.21*	*0.01*
(T)²	0.14	−0.09	0.15	**0.13**	0.11	−0.09	−0.11	−0.10	0.14	−0.08
	0.05	*0.18*	*0.03*	***0.07***	*0.10*	*0.18*	*0.10*	*0.14*	*0.05*	*0.27*
(P)²	−0.11	0.05	−0.13	**−0.09**	−0.08	0.05	0.08	0.07	−0.11	0.03
	0.13	*0.46*	*0.07*	***0.18***	*0.26*	*0.46*	*0.26*	*0.35*	*0.13*	*0.67*
(Q)²	0.16	−0.06	0.20	**0.14**	0.11	−0.06	−0.11	−0.09	0.16	−0.02
	0.02	*0.39*	*0.00*	***0.05***	*0.11*	*0.39*	*0.11*	*0.22*	*0.02*	*0.79*

Note: Italicized numbers are the *p*-values of correlation and bold letters are variables selected for construction of the regression model.

All variables of Model E are significant, with *p*-values of zero and VIF between 1.0 and 1.62. Moreover, the Prediction Errors (PRESS) for Model E are the smallest and the F statistics the highest among all models. Therefore, Model E was further subjected to stepwise and best-subset regression analyses to further examine the principal factors affecting VR, as explained in the methodology. The regression statistics remain the same as in Model E, suggesting it to be the best regression model for estimating VR. Therefore, Model E is designated henceforth as Model 2 (M2; Equation (7); Figure 12).

$$\sqrt{V} = 6.43 + 0.00079\ VT - 1.96\ ln(AOD) - 2.30\ ln(RH) + 0.017\ Q^2 \qquad (7)$$

Table 3. Multiple linear regression models for predicting $(VR)^2$. The final model selected for estimating $(VR)^2$ is highlighted.

Model	Const	UT	VT	U	V	ln(AOD)	ln(RH)	$(T)^2$	$(P)^2$	$(Q)^2$	S	R^2	R^2_{adj}	PRESS	R^2_{pred}	SS	F	DWS	Largest VIF	Cp
Full	ns	ns	ns	ns	ns	****	****	ns	ns	***	0.34	72.38	70.97	24.33	69.50	57.74	51.37	1.69	68.52	x
A	ns	ns	ns	*	ns	****	****	x	ns	****	0.33	72.34	71.07	24.09	69.79	57.71	57.24	1.69	65.43	x
B	****	*	ns	*	ns	****	****	x	x	****	0.33	72.31	71.20	23.84	70.11	57.69	64.65	1.68	66.73	x
C	****	**	***	**		****	****	x	x	****	0.33	71.79	70.94	23.91	70.03	57.26	84.82	1.66	35.28	x
D	****	x	***	ns		****	****	x	x	****	0.33	71.21	70.49	24.20	69.64	56.81	99.40	1.66	1.62	x
E	****	**x**	****	**x**		****	****	**x**	**x**	****	**0.33**	**71.10**	**70.53**	**24.07**	**69.83**	**56.71**	**124.20**	**1.67**	**1.62**	**x**
Stepwise	****	x	****	x		****	****	x	x	****	0.33	71.10	70.53	24.01	69.83	x	x	x	x	5
Best Subset	****	x	****	x		****	****	x	x	****	0.33	71.10	70.53	x	x	x	x	x	x	5

Note: Significance levels are as follows: ****—$p < 0.001$; ***—$p < 0.01$; **—$p < 0.05$; *—$p < 0.1$; ns—not significant. X—N/A and variable excluded from regression, Const—Intercept of regression model. "Full" refers to the multiple linear regression models involving all parameters, F: F-statistic, PRESS: Error in prediction, SS: Sum of Squares, MS: Mean Square, R^2_{pred}: Predicted coefficient of determination, DWS: Durban Watson Statistics, VIF: Variance Inflation Factor.
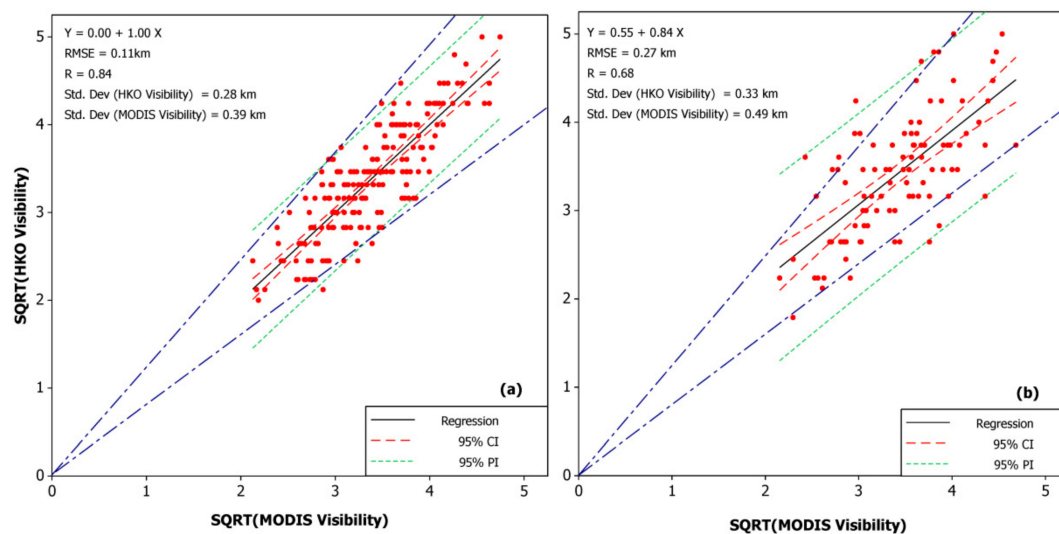
Figure 12. Correlation between Square root of MODIS visibility at HKO (SQRT (MODIS Visibility)) and Square root of ground visibility at HKO (SQRT (HKO Visibility)) using M2 (**a**) linear multiple regression of training data for the years 2005 to 2007; (**b**) simulated MODIS visibility using validation of data (MODIS AOD and Climatic data) from years 2008. Blue dotted dashed lines show the upper and lower limit of ±20% of the ground visibility at HKO, whereas black solid line is the resultant regression line.

With the addition of climate parameters exhibiting a significant relationship with VR, M2 (Equation (7)) actually performs better than M1, with significantly higher values of R = 84%, R^2 = 71.1%, a predicted-R^2 of 69.8%, and a lower RMSE = 0.11 km (Figure 12a). It should be noted that among the training data sets, the years 2002 and 2006 were much drier than average years, 2007 was wetter than normal, and 2006 was an El-Nino year, but model M2 was still able to capture the considerable variability within the data (Figure 12a). Furthermore, M2 is also capable of simulating real-time VR at HKO with high accuracy, as demonstrated by a low RMSE of 0.27 km (Figure 12b).

The new model is able to represent the synergism between the physical forces influencing VR in terms of the dynamic interactions between air density, turbulence and advection. Respective signs (+ and −) for the coefficients of M2 suggest that a unit increase in any one or combination of "VT" and "Q" also increases the visibility, whereas a unit increase in ln(AOD) and/or "RH" decreases the visibility. This is also in agreement with the physical forces explained in the section "Time Series Analysis".

Although ln(RH) has the highest coefficient in Equation (7) as per the F-statistic, M2 is highly sensitive to changes in ln(AOD), with an F-value of 401, followed by Q^2, ln(RH) and VT, with F-values of 41.10, 28.24 and 10.57, respectively. This may be because Q depends on P, T and RH, and therefore acts as a compound variable whose interaction with VR can also explain the combined effect of P, T and RH on VR. The performance of M2 also suggests that VT is sufficient to explain the effects of WS and WD on the dispersion of aerosols, and hence on VR. The presence of VT, RH and Q in a model can also increase the multicollinearity, although DWS values close to one for M2 (Table 2), suggest no multicollinearity in M2. This explains why M2 is able to accurately estimate VR at HKO, as shown by the summary statistics of real-time and simulated VR at HKO for the year 2008 (Table 4).

Eighty-one percent of the simulated cases for VR using M2 are found to also be within ±20% of the HKO VR (Figures 12 and 13), which is consistent with Annex 3 of the International Civil Aviation Organization (ICAO), which suggests that an uncertainty of ±20% in estimated VR is acceptable when actual VR is above 1.5 km.

Table 4. Summary statistics for the real-time (HKO VR) and simulated (MODIS VR) VR at HKO for the year 2008.

Test	HKO VR (km)	MODIS VR (km)
Total observations	95	95
Mean	12.25	12.10
Standard Error	0.51	0.40
Median	12.00	12.18
Maximum	25.00	21.93
Minimum	3.20	4.64
Standard Deviation	0.33	0.49
First Quartile	9.00	9.08
Third Quartile	15.00	14.87
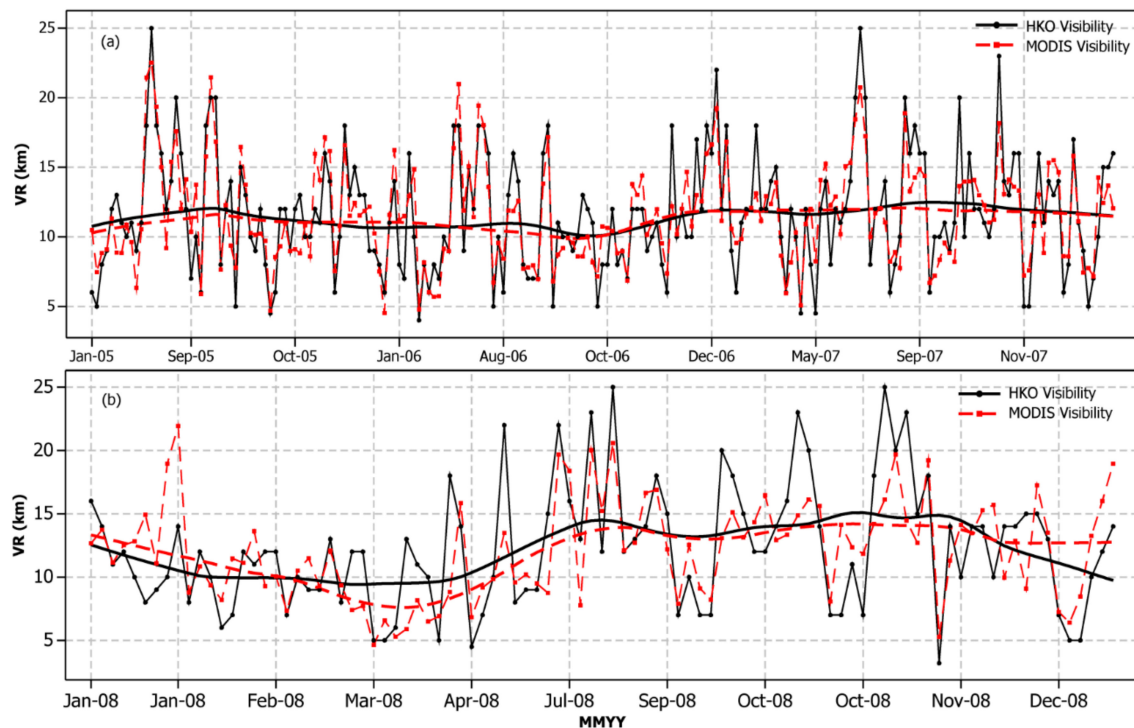
Figure 13. Time series of the real-time and simulated VR at HKO using Model 2 for the (**a**) Training data set of 2005–2007; and (**b**) Validation data set of 2008. Black solid line and dotted red line show the smoothed trend line for HKO and MODIS visibility, respectively.

To further consolidate the results of this study, we further validated the proposed model M2 (Equation (7)) at HKIA using MODIS AOD and climatic data over HKIA (Figure 14). Model M2 performed significantly well, reproducing the variations in the observed VR at HKIA with a high correlation of 0.77 and a reasonable error of 3.57 km. We also tested another model using AOD of MISR and climatic data over HKO; as reported in the previous section, the statistics were better than for MODIS. However, this new model (Equation (8); Figure 15) for MISR did not perform better than MODIS (M2; Equation (7); Figure 12), and showed R^2 = 59.91%, a predicted-R^2 of 39.89% and high overestimation error (RMSE = 22.77 km) (Figure 15). The inferior result may be due to the reasons explained in Section 3.2.

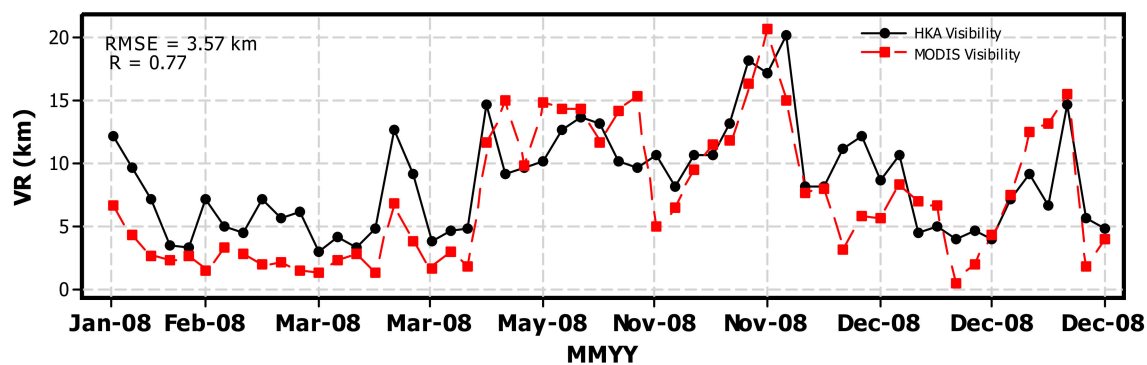$$\sqrt{B_{ext}} = 17.35 + 0.312\,AOD - \frac{17249}{P} + 0.0002Q^2 \tag{8}$$

Figure 14. Time series of real-time and simulated VR at HKIA from Model 2 for the validation data set (MODIS AOD and climatic data) of 2008 over HKIA.
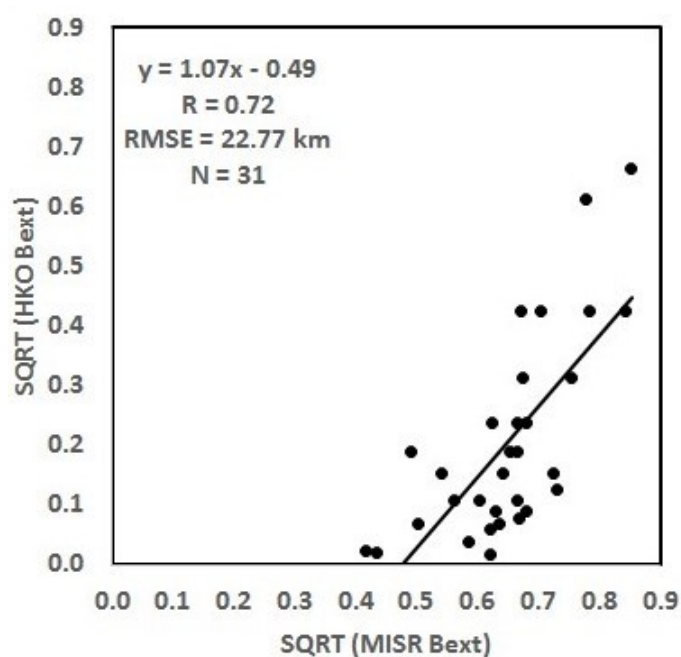

Figure 15. Correlation between Square root of MISR B_{ext} and Square root of ground visibility at HKO using Equation (7) for 2005 to 2008. Black solid line is the resultant regression line and N is the total number of observations.

4. Discussion

The results of this study, with an R of 0.84, are considerably better than previous studies on visibility estimation for Hong Kong and the Chinese mainland (Table 5). These have used expensive and time-consuming methods combining mass pollutant concentrations, along with available meteorological data. They have also used averaged daily data, which cannot serve real-time operational purposes, which may explain the large bias, especially for clear or very polluted days. The use of satellite-derived AOD along with time-matched hourly meteorological data giving wind flux conditions at different heights in this study appears to be complementary, with the wind profiler data compensating for the whole-column readings of the satellite AOD. Thus, this study has achieved better matching with ground station visibility data.

Table 5. Results of the previous studies on the same topic for Hong Kong and mainland China.

	Dependent Variable	Independent Variables	R^2
Lai and Sequeira [64]	B_{ext}	NO_2, RSP, RH	0.76
Du et al. [43]	VR	RH, WS, P, T, Prec.	0.39
Mui et al. [33]	VR	T, API	0.77
Lin et al. [53]	VR	PM_{10}, NO_2, RH	0.80
Wan et al. [65]	VR	SO_2, NO_2, PM_{10}	0.51

Note: RSP—Respirable Suspended Particles; Prec.—Precipitation; API—Air Pollution Index.

As the correlations, RMSE and MAD for MISR AOD and B_{ext} were good for both MODIS and MISR, both sensors' AOD products were used along with climatic data to develop numerical models. However, the model from MODIS achieved better estimations when validated against ground station visibility and, due to its higher temporal resolution of 1-day, shows greater potential for operational use.

It is notable that for all sensors except for OMI with kernel window of 1-by-1, or 28 km resolution, the highest resolution for each sensor did not achieve the best result compared to ground-level VR. The best results, obtained by the MODIS window size of 5-by-5 (50 km) and the MISR window size of 3-by-3 (52 km), suggest that a resolution of approximately 50 km is optimal for satellite-based remote sensing of VR. This may be because the larger window sizes deal better with cloud contamination, as cloud masking detects spatial variability within pixel blocks, which is more effective with larger block sizes.

5. Conclusions

Point-based observations from ground instruments cannot be used to produce regional composites in surface-level VR over urban industrial regions due to the inhomogeneity of aerosol loading in these areas. Moreover, recently developed and current satellite-based models parameterized with satellite-based AOD alone have proven ineffective at simulating surface-level VR. Additionally, there has been no previous evaluation of the potential of AOD from different satellite sensors for estimation of surface-level VR. This study was designed to develop an operational model for the estimation of surface-level VR over a complex urban and industrial region using the most suitable satellite-based AOD product.

Among AOD products from MODIS, MISR, OMI and CALIOP, the highest correlation of AOD with B_{ext} at HKIA was found for MISR with an observational kernel window of 1-by-1 (17.5 km) (R = 0.60), followed by MISR AOD for kernel windows of 3-by-3 (52 km) (R = 0.51). The highest correlation at HKO was for MISR AOD for a kernel window of 3-by-3 (52 km) (R = 0.63), followed by MODIS AOD with a kernel window of 5-by-5 (50 km) (R = 0.53). Our proposed model, using MODIS AOD with climatic data, estimated surface-level VR with high accuracy (i.e., R = 0.84, RMSE = 0.11 km and slope = 1.0). The results of this study suggest that Q alone can explain the combined effect of P, T and RH on VR. The results also suggest that VT alone is sufficient to explain the effects of T, WS and WD on the dispersion of aerosols and, hence, on VR. The proposed model is the first to simulate surface-level VR under variable aerosol loading and climate conditions using satellite-based AOD.

The results of this study demonstrate the potential for applying passive satellite depictions of broad-scale aerosol optical properties to fill data gaps in Hong Kong that arise due to relatively coarse deployment of ground instruments for visibility monitoring. The best results obtained with 50 km spatial resolution would be operational for regional visibility monitoring in the Hong Kong and Pearl River Delta region, where regional airports and shipping require accurate visibility data. However, within Hong Kong, ground stations may still be the best option until higher-resolution sensors become available. The results of the study will help to understand the dynamics of spatiotemporal changes in the optical properties and visibility of regional aerosols. They could also help to study the impact of air pollution on health and weather on a regional scale.

References

1. Total, A.; Year, A.T. *Number of Hours of Reduced Visibility Observed at the Hong Kong Observatory Since 1968*; Hong Kong Observatory: Tsim Sha Tsui, Hong Kong, 1968.

2. Wong, M.S.; Lee, K.H.; Nichol, J.E. Estimation of aerosol sources and aerosol transport pathways using AERONET clustering and backward trajectories: A case study of Hong Kong. *Int. J. Remote Sens.* **2013**, *34*, 938–955. [CrossRef]

3. Chan, C.K.; Yao, X. Air pollution in mega cities in China. *Atmos. Environ.* **2008**, *42*, 1–42. [CrossRef]

4. Lee, Y.C.; Hills, P.R. Cool season pollution episodes in Hong Kong, 1996–2002. *Atmos. Environ.* **2003**, *37*, 2927–2939. [CrossRef]

5. Ho, K.; Lee, S.; Chan, C.K.; Yu, J.C.; Chow, J.C.; Yao, X. Characterization of chemical species in PM2.5 and PM10 aerosols in Hong Kong. *Atmos. Environ.* **2003**, *37*, 31–39. [CrossRef]

6. Xiao, F.; Brajer, V.; Mead, R.W. Blowing in the wind: The impact of China's Pearl River Delta on Hong Kong's air quality. *Sci. Total Environ.* **2006**, *367*, 96–111. [CrossRef] [PubMed]

7. Lyamani, H.; Olmo, F.J.; Alados-Arboledas, L. Physical and optical properties of aerosols over an urban location in Spain: Seasonal and diurnal variability. *Atmos. Chem. Phys.* **2010**, *10*, 239–254. [CrossRef]

8. Devara, P.C.S.; Kumar, S.; Pandithurai, G.; Safai, P.D.; Dipu, S. Comparison between urban aerosol products retrieved from collocated Cimel and Prede Sun/sky radiometers at Pune, India. *Meteorol. Atmos. Phys.* **2013**, *120*, 189–200. [CrossRef]

9. Horvath, H. The University of Vienna telephotometer. *Atmos. Environ.* **1981**, *15*, 2537–2546. [CrossRef]

10. Han, Y.; Lu, D.; Rao, R.Z.; Wang, Y.J. Determination of the complex refractive indices of aerosol from aerodynamic particle size spectrometer and integrating nephelometer measurements. *Appl. Opt.* **2009**, *48*, 4108–4117. [CrossRef] [PubMed]

11. Watson, J.G. Visibility: Science and regulation. *J. Air Waste Manag. Assoc.* **2002**, *52*, 628–713. [CrossRef] [PubMed]

12. Bian, Q. *Study of Visibility Degradation over the Pearl River Delta Region: Source Apportionment and Impact of Chemical Characteristics*; Hong Kong University of Science and Technology: Clear Water Bay, Hong Kong, 2011.

13. Henry, R.C. A field study of visual perception of complex natural targets through atmospheric haze by naïve observers. *Atmos. Environ.* **2006**, *40*, 5251–5261. [CrossRef]

14. Anderson, T.L.; Masonis, S.J.; Covert, D.S.; Ahlquist, N.C.; Howell, S.G.; Clarke, A.D.; McNaughton, C.S. Variability of aerosol optical properties derived from in situ aircraft measurements during ACE-Asia. *J. Geophys. Res.* **2003**, *108*, 15–19. [CrossRef]

15. Pikridas, M.; Sciare, J.; Freutel, F.; Crumeyrolle, S.; Von Der Weiden-Reinmüller, S.-L.; Borbon, A.; Schwarzenboeck, A.; Merkel, M.; Crippa, M.; Kostenidou, E.; et al. In situ formation and spatial variability of particle number concentration in a European megacity. *Atmos. Chem. Phys.* **2015**, *15*, 10219–10237. [CrossRef]

16. Zhao, T.; Liu, D.; Zheng, X.; Yang, L.; Gu, X.; Hu, J.; Shu, Z.; Chang, J.; Wu, X. Revealed variations of air quality in industrial development over a remote plateau of Southwest China: An application of atmospheric visibility data. *Meteorol. Atmos. Phys.* **2017**, *129*, 659–667. [CrossRef]

17. Mishchenko, M.I.; Geogdzhayev, I.V.; Liu, L.; Ogren, J.A.; Lacis, A.A.; Rossow, W.B.; Hovenier, J.W.; Volten, H.; Muñoz, O. Aerosol retrievals from AVHRR radiances: Effects of particle nonsphericity and absorption and an updated long-term global climatology of aerosol properties. *J. Quant. Spectrosc. Radiat. Transf.* **2003**, *79–80*, 953–972. [CrossRef]

18. Bendix, J. Determination of fog horizontal visibility by means of NOAA-AVHRR. In *1995 International Geoscience and Remote Sensing Symposium, IGARSS '95. Quantitative Remote Sensing for Science and Applications*; IEEE: Piscataway, NJ, USA, 1995; Volume 3, pp. 1847–1849.

19. Williams, D.H.; Cogan, J.L. Estimation of visibility from satellite imagery. *Appl. Opt.* **1991**, *30*, 414–419. [CrossRef] [PubMed]

20. Nichol, J.E.; Wong, M.S.; Wang, J. A 3D aerosol and visibility information system for urban areas using remote sensing and GIS. *Atmos. Environ.* **2010**, *44*, 2501–2506. [CrossRef]

21. Hadjimitsis, D.G.; Clayton, C.; Toulios, L. Retrieving visibility values using satellite remote sensing data. *Phys. Chem. Earth Parts A/B/C* **2010**, *35*, 121–124. [CrossRef]

22. Fei, H.; Hong, W.; Junping, Q.; Guofu, W. Retrieval of atmospheric horizontal visibility by statistical regression from NOAA/AVHRR satellite data. *J. Ocean Univ. China* **2006**, *5*, 207–212. [CrossRef]

23. Shahzad, M.I.; Nichol, J.E.; Wang, J.; Campbell, J.R.; Chan, P.W. Estimating surface visibility at Hong Kong from ground-based LIDAR, sun photometer and operational MODIS products. *J. Air Waste Manag. Assoc.* **2013**, *63*, 1098–1110. [CrossRef] [PubMed]

24. He, Q.; Li, C.; Geng, F.; Zhou, G.; Gao, W.; Yu, W.; Li, Z.; Du, M. A parameterization scheme of aerosol vertical distribution for surface-level visibility retrieval from satellite remote sensing. *Remote Sens. Environ.* **2016**, *181*, 1–13. [CrossRef]

25. Rozwadowska, A. Influence of aerosol vertical profile variability on retrievals of aerosol optical thickness from NOAA AVHRR measurements in the Baltic region. *Oceanologia* **2007**, *49*, 165–184.

26. Wilson, R.T.; Milton, E.J.; Nield, J.M. Are visibility-derived AOT estimates suitable for parameterizing satellite data atmospheric correction algorithms? *Int. J. Remote Sens.* **2015**, *36*, 1675–1688. [CrossRef]

27. Koschmieder, H. Theorie der Horizontalen Sichtweite. *Beitr. Phys. Frei. Atmos.* **1924**, *12*, 33–53.

28. Kessner, A.L.; Wang, J.; Levy, R.C.; Colarco, P.R. Remote sensing of surface visibility from space: A look at the United States East Coast. *Atmos. Environ.* **2013**, *81*, 136–147. [CrossRef]

29. Bilal, M.; Nazeer, M.; Nichol, J.E. Validation of MODIS and VIIRS derived aerosol optical depth over complex coastal waters. *Atmos. Res.* **2017**, *186*, 43–50. [CrossRef]

30. Bilal, M.; Nichol, J.E.; Chan, P.W. Validation and accuracy assessment of a Simplified Aerosol Retrieval Algorithm (SARA) over Beijing under low and high aerosol loadings and dust storms. *Remote Sens. Environ.* **2014**, *153*, 50–60. [CrossRef]

31. Bilal, M.; Nichol, J.E. Evaluation of MODIS aerosol retrieval algorithms over the Beijing-Tianjin-Hebei region during low to very high pollution events. *J. Geophys. Res. Atmos.* **2015**, *120*, 7941–7957. [CrossRef]

32. Toth, T.D.; Zhang, J.; Campbell, J.R.; Hyer, E.J.; Reid, J.S.; Shi, Y.; Westphal, D.L. Impact of data quality and surface-to-column representativeness on the $PM_{2.5}$/satellite AOD relationship for the contiguous United States. *Atmos. Chem. Phys.* **2014**, *14*, 6049–6062. [CrossRef]

33. Mui, K.W.; Wong, L.T.; Chung, L.Y. Mathematical models for accurate prediction of atmospheric visibility with particular reference to the seasonal and environmental patterns in Hong Kong. *Environ. Monit. Assess.* **2009**, *158*, 333–341. [CrossRef] [PubMed]

34. Remer, L.A.; Kaufman, Y.J.; Tanré, D.; Mattoo, S.; Chu, D.A.; Martins, J.V.; Li, R.-R.; Ichoku, C.; Levy, R.C.; Kleidman, R.G.; et al. The MODIS Aerosol Algorithm, Products, and Validation. *J. Atmos. Sci.* **2005**, *62*, 947–973. [CrossRef]

35. Diner, D.J.; Beckert, J.C.; Reilly, T.H.; Bruegge, C.J.; Conel, J.E.; Kahn, R.A.; Martonchik, J.V.; Ackerman, T.P.; Davies, R.; Gerstl, S.A.W.; et al. Multi-angle Imaging SpectroRadiometer (MISR) instrument description and experiment overview. *IEEE Trans. Geosci. Remote Sens.* **1998**, *36*, 1072–1087. [CrossRef]

36. Torres, O. Total Ozone Mapping Spectrometer measurements of aerosol absorption from space: Comparison to SAFARI 2000 ground-based observations. *J. Geophys. Res.* **2005**, *110*. [CrossRef]

37. Winker, D.M.; Pelon, J.; Coakley, J.A.; Ackerman, S.A.; Charlson, R.J.; Colarco, P.R.; Flamant, P.; Fu, Q.; Hoff, R.M.; Kittaka, C.; et al. The CALIPSO Mission: A Global 3D View of Aerosols and Clouds. *Bull. Am. Meteorol. Soc.* **2010**, *91*, 1211–1229. [CrossRef]

38. Livingston, J.M.; Redemann, J.; Russell, P.B.; Torres, O.; Veihelmann, B.; Veefkind, P.; Braak, R.; Smirnov, A.; Remer, L.; Bergstrom, R.W.; et al. Comparison of aerosol optical depths from the Ozone Monitoring Instrument (OMI) on Aura with results from airborne sunphotometry, other space and ground measurements during MILAGRO/INTEX-B. *Atmos. Chem. Phys.* **2009**, *9*, 6743–6765. [CrossRef]

39. Kahn, R.A. Multiangle Imaging Spectroradiometer (MISR) global aerosol optical depth validation based on 2 years of coincident Aerosol Robotic Network (AERONET) observations. *J. Geophys. Res.* **2005**, *110*. [CrossRef]

40. Omar, A.H.; Winker, D.M.; Tackett, J.L.; Giles, D.M.; Kar, J.; Liu, Z.; Vaughan, M.A.; Powell, K.A.; Trepte, C.R. CALIOP and AERONET aerosol optical depth comparisons: One size fits none. *J. Geophys. Res. Atmos.* **2013**, *118*, 4748–4766. [CrossRef]

41. Wong, M.S.; Nichol, J.; Lee, K.H.; Li, Z. A New Algorithm for Retrieving Aerosol Optical Thickness Using TERRA/MODIS Satellite Images. *Geogr. Inf. Sci.* **2008**, *14*, 86–91. [CrossRef]

42. Zhang, Q.; Ning, Z.; Shen, Z.; Li, G.; Zhang, J.; Lei, Y.; Xu, H.; Sun, J.; Zhang, L.; Westerdahl, D.; et al. Variations of aerosol size distribution, chemical composition and optical properties from roadside to ambient environment: A case study in Hong Kong, China. *Atmos. Environ.* **2017**, *166*, 234–243. [CrossRef]

43. Du, K.; Mu, C.; Deng, J.; Yuan, F. Study on atmospheric visibility variations and the impacts of meteorological parameters using high temporal resolution data: An application of Environmental Internet of Things in China. *Int. J. Sustain. Dev. World Ecol.* **2013**, *20*, 238–247. [CrossRef]

44. Seinfeld, J.H.; Pandis, S.N. *Atmospheric Chemistry and Physics: From Air Pollution to Climate Change*, 2nd ed.; John Wiley & Sons, Inc.: Hoboken, NJ, USA, 2006; ISBN 9780471720188.

45. Chang, D.; Song, Y.; Liu, B. Visibility trends in six megacities in China 1973–2007. *Atmos. Res.* **2009**, *94*, 161–167. [CrossRef]

46. Lee, Y.C.; Savtchenko, A.; Council, G.; Kong, H. Relationship between air pollution in Hong Kong and in the Pearl River Delta region of South China 2003 and 2004: An analysis. *J. Appl. Meteorol. Climatol.* **2006**, *45*, 269–282. [CrossRef]

47. Zhou, W.; Li, R.C.Y.; Chow, E.C.H.; Zhou, W.; Li, R.C.Y. Intraseasonal Variation of Visibility in Hong Kong. *Adv. Atmos. Sci.* **2017**, *34*, 26–38. [CrossRef]

48. Wu, D.; Tie, X.; Li, C.; Ying, Z.; Lau, A.K.-H.; Huang, J.; Deng, X.; Bi, X. An extremely low visibility event over the Guangzhou region: A case study. *Atmos. Environ.* **2005**, *39*, 6568–6577. [CrossRef]

49. Campbell, J.R.; Reid, J.S.; Westphal, D.L.; Zhang, J.; Tackett, J.L.; Chew, B.N.; Welton, E.J.; Shimizu, A.; Sugimoto, N.; Aoki, K.; et al. Characterizing the vertical profile of aerosol particle extinction and linear depolarization over Southeast Asia and the Maritime Continent: The 2007–2009 view from CALIOP. *Atmos. Res.* **2013**, *122*, 520–543. [CrossRef]

50. Ichoku, C.; Chu, D.A.; Mattoo, S.; Kaufman, Y.J.; Remer, L.A.; Tanré, D.; Slutsker, I.; Holben, B.N. A spatio-temporal approach for global validation and analysis of MODIS aerosol products. *Geophys. Res. Lett.* **2002**, *29*, MOD1-1–MOD1-4. [CrossRef]

51. Anderson, T.W.; Darling, D.A. A Test of Goodness of Fit. *J. Am. Stat. Assoc.* **1954**, *49*, 765–769. [CrossRef]

52. Durbin, J.; Watson, G.S. Testing for serial correlation in least squares regression. III. *Biometrika* **1971**, *58*, 1–19. [CrossRef]

53. Lin, M.; Tao, J.; Chan, C.-Y.; Cao, J.-J.; Zhang, Z.-S.; Zhu, L.-H.; Zhang, R.-J. Regression Analyses between Recent Air Quality and Visibility Changes in Megacities at Four Haze Regions in China. *Aerosol Air Qual. Res.* **2012**, *12*, 1049–1061. [CrossRef]

54. Hudak, A.T.; Crookston, N.L.; Evans, J.S.; Falkowski, M.J.; Smith, A.M.; Gessler, P.E.; Morgan, P. Regression modeling and mapping of coniferous forest basal area and tree density from discrete-return lidar and multispectral satellite data. *Can. J. Remote Sens.* **2006**, *32*, 126–138. [CrossRef]

55. Mallows, C.L. Some Comments on CP. *Technometrics* **1973**, *15*, 661–675.

56. Curier, R.L.; Veefkind, J.P.; Braak, R.; Veihelmann, B.; Torres, O.; de Leeuw, G. Retrieval of aerosol optical properties from OMI radiances using a multiwavelength algorithm: Application to western Europe. *J. Geophys. Res.* **2008**, *113*. [CrossRef]

57. Min, M.; Wang, P.; Campbell, J.R.; Zong, X.; Li, Y. Midlatitude cirrus cloud radiative forcing over China. *J. Geophys. Res.* **2010**, *115*, D20210. [CrossRef]

58. Torres, O.; Bhartia, P.K.; Herman, J.R.; Ahmad, Z.; Gleason, J. Derivation of aerosol properties from satellite measurements of backscattered ultraviolet radiation: Theoretical basis. *J. Geophys. Res.* **1998**, *103*, 17099–17110. [CrossRef]

59. Hidy, G.; Hoff, R.; Christopher, S.; Sharma, P.; Poulsen, T.; Kalluri, P.; Hoff, S.; Bundy, D.; Nelson, M.; Zelle, B.; et al. The A&WMA 2009 Critical Review—Remote Sensing of Particulate Pollution from Space: Have We Reached the Promised Land? *J. Air Waste Manag. Assoc.* **2009**, *59*, 645–675. [CrossRef]

60. Kacenelenbogen, M.; Vaughan, M.A.; Redemann, J.; Hoff, R.M.; Rogers, R.R.; Ferrare, R.A.; Russell, P.B.; Hostetler, C.A.; Hair, J.W.; Holben, B.N. An accuracy assessment of the CALIOP/CALIPSO version

2/version 3 daytime aerosol extinction product based on a detailed multi-sensor, multi-platform case study. *Atmos. Chem. Phys.* **2011**, *11*, 3981. [CrossRef]

61. Liu, J.; Xia, X.; Li, Z.; Wang, P.; Min, M.; Hao, W.; Wang, Y.; Xin, J.; Li, X.; Zheng, Y.; et al. Validation of multi-angle imaging spectroradiometer aerosol products in China. *Tellus B Chem. Phys. Meteorol.* **2010**, *62*, 117–124. [CrossRef]

62. Jiang, X.; Liu, Y.; Yu, B.; Jiang, M. Comparison of MISR aerosol optical thickness with AERONET measurements in Beijing metropolitan area. *Remote Sens. Environ.* **2007**, *107*, 45–53. [CrossRef]

63. Kahn, R.; Banerjee, P.; McDonald, D. Sensitivity of multiangle imaging to natural mixtures of aerosols over ocean. *J. Geophys. Res.* **2001**, *106*, 18219–18238. [CrossRef]

64. Lai, L.Y.; Sequeira, R. Visibility degradation across Hong Kong: Its components and their relative contributions. *Atmos. Environ.* **2001**, *35*, 5861–5872. [CrossRef]

65. Wan, J.-M.; Lin, M.; Chan, C.-Y.; Zhang, Z.-S.; Engling, G.; Wang, X.-M.; Chan, I.-N.; Li, S.-Y. Change of air quality and its impact on atmospheric visibility in central-western Pearl River Delta. *Environ. Monit. Assess.* **2011**, *172*, 339–351. [CrossRef] [PubMed]